Journal of Marine Science and Application (2018) 17:297–311
https://doi.org/10.1007/s11804-018-0043-3

RESEARCH ARTICLE

Radiation and Exciting Forces of Axisymmetric Structures with a Moonpool in Waves

Keynote Contribution for the International Workshop on Wave Loads and Motions of Ships and Offshore Structures, Harbin, China, 5-7 November, 2017

Ronald W. Yeung[1] · **Lu Wang**[1]

Received: 3 June 2018 / Accepted: 22 July 2018 / Published online: 25 September 2018

Abstract

A highly efficient "hybrid integral-equation method" for computing hydrodynamic added-mass, wave-damping, and wave-exciting force of general body geometries with a vertical axis of symmetry is presented. The hybrid method utilizes a numerical inner domain and a semi-infinite analytical outer domain separated by a vertical cylindrical matching boundary. Eigenfunction representation of velocity potential is used in the outer domain; the three-dimensional potential in the inner domain is solved using a "two-dimensional" boundary element method with ring sources and ring dipoles to exploit the body symmetry for efficiency. With proper solution matching at the common boundary, both radiation and diffraction potentials can be solved efficiently while satisfying the far-field radiation condition exactly. This method is applied to compute the hydrodynamic properties of two different body geometries: a vertical-walled moonpool with a bottom plate that restricts the opening and a spar-like structure with a diverging bottom opening inspired by designs of floating Oscillating Water Columns. The effects of the size of the bottom opening on the hydrodynamic properties of the body are investigated for both geometries. The heave motion of the floater as well as the motion of the internal free surface under incident wave excitation are computed and studied for the spar-like structure.

Keywords Moonpool · Spar · Oscillating water column · Potential flow · Hybrid method · Axisymmetric body

1 Introduction

Moonpools have been extensively utilized in various marine applications ranging from drilling to underwater exploration. The resonance of the internal moonpool free surface is highly complex and has been the subject of extensive research over the past decades. Traditionally, the research on moonpool behavior is carried out using various methods based on the linearized potential-flow theory. The method of matched eigenfunctions is very convenient for relatively simple body geometries involving vertical and horizontal surfaces. For instance, the hydrodynamic coefficients of a truncated vertical cylinder (Yeung 1981) and, in a more complicated case, that of a coaxial-cylinder wave-energy device have been efficiently computed using this method (Chau and Yeung 2012; Wang et al. 2016). In the context of moonpools, the method of matched eigenfunctions has been successfully applied to identify moonpool resonance frequencies and mode shapes without external free surface (Molin 2001; Molin et al. 2018). The same method can also be easily adapted to incorporate free surface external to the moonpool wall in both two dimensions (Yeung and Seah 2007) and three dimensions (Mavrakos 1988, 2004; Shipway and Evans 2003). More recently, the method of matched eigenfunctions has been successfully applied to study moonpools containing a two-layer fluid (Zhang and Bandyk 2013, 2014). Alternatively, the potential-flow problem with moonpools can be solved numerically using a panel method with the free-surface Green's function (wave sources). This approach is more versatile when dealing with complex body geometries and was applied extensively to study trapped modes

✉ Ronald W. Yeung
rwyeung@berkeley.edu

[1] Department of Mechanical Engineering, University of California at Berkeley, Berkeley, CA 94720-1740, USA

(Newman 1999; McIver 2005; McIver and McIver 2007). However, without using additional panels to "cap" the solid body, the wave-source formulation leads to many irregular frequencies with nonphysical resonance. This issue greatly complicates the study of moonpools which also have many physical internal resonance frequencies.

Despite their usefulness in studying moonpool behavior, potential-flow methods tend to significantly over-predict the moonpool wave amplitude near resonance (Faltinsen et al. 2007). The discrepancy is at least partly caused by a lack of viscous damping which can be significant if the moonpool wall features sharp edges. One obvious approach to resolve this issue is to perform viscous Computational Fluid Dynamics (CFD) simulations. It has been demonstrated that potential-flow solvers can be effectively combined with Navier-Stokes solvers to more efficiently simulate moonpool behaviors with viscous effects (Kristiansen and Faltinsen 2012; Kristiansen et al. 2013; Fredriksen et al. 2014). This task is made slightly easier by the fact that viscous effects primarily manifest in the form of flow separation near sharp edges which does not require very high numerical resolution to properly capture. Alternatively, some empirical correction can be made to potential-flow simulations to improve the prediction of the magnitude of moonpool resonance (Faltinsen and Timokha 2015). Nevertheless, an efficient and robust boundary element method based on potential-flow theory is still likely the preferred approach to conduct large parametric studies for various moonpool designs, especially in three dimensions, partly because of its computational efficiency and partly because of the ease of creating meshes. The inviscid solutions are still highly valuable in terms of approximately identifying the various internal resonance frequencies of the moonpool and providing, away from resonances, a quantitative baseline for further CFD simulations.

This paper presents a highly efficient hybrid integral-equation method for solving the potential-flow problem about arbitrary body or bodies with a vertical axis of symmetry in waves. This hybrid method utilizes a numerical inner domain containing the body and a semi-infinite analytical outer domain separated by a vertical cylindrical matching boundary. Eigenfunction representation of the velocity potentials is utilized in the outer domain while the three-dimensional potential in the inner domain is solved using a "two-dimensional" boundary element method with ring sources and dipoles to exploit the body symmetry for efficient computation. The two-dimensional version of this hybrid method is originally presented by Yeung (1975) and later applied to steady ship waves (Yeung and Bouger 1979). This method is later extended to general three-dimensional bodies without symmetry (Yuen and Chau 1987; Matsui et al. 1987; Matsui and Kato 1991) and to time-domain problems (Yeung 1985; Lee 1985; Hamilton and Yeung 2003). In this paper, we focus on the application of the hybrid integral-equation method to the radiation and diffraction problems of two different axisymmetric bodies with circular moonpools: a thick-walled moonpool with a bottom plate of restricted opening and a spar-shaped structure with a diverging bottom opening inspired by designs of floating Oscillating Water Columns (OWCs) (Falcão et al. 2012). The fact that the current method is free from irregular frequencies greatly facilitates the analysis of the results. Furthermore, the body motion and moonpool behavior when the body is heaving under the excitation of incident waves are also investigated.

2 Description of the Hydrodynamic Problem

The current work focuses on the computation of the radiation and diffraction potentials about an axisymmetric surface-piercing structure with a moonpool in the center. The radiation and wave excitation forces on the structure as well as the fluid motion inside the moonpool will also be deduced from the solutions of the potentials. As an example, a vertical thick-walled moonpool with a bottom plate that restricts the opening is shown in Fig. 1.

The hybrid integral-equation method employed in this paper requires the separation of the flow domain $\mathcal{D}$ into two parts: an inner domain $\mathcal{D}^{(i)}$ and an outer domain $\mathcal{D}^{(o)}$. The two domains are separated by a cylindrical matching boundary Σ_C of radius R_C. The boundary Σ_C also separates the calm free surface located at $y = 0$ into $\Sigma_F^{(o)}$, the section in the outer domain, and $\Sigma_F^{(i)}$ for the part in the inner domain which also includes the moonpool free surface for convenience. The flat bottom surface Σ_B is located at $y = -h$ with h being the water depth. The surface of the body at the equilibrium position is denoted by S_B. Driven by incident waves of amplitude A and wave number k_0, the structure exhibits time-harmonic oscillations about its equilibrium position. Only heave motion with complex amplitude A_2 is considered here, although the current method can be easily extended to investigate surge and pitch motions as well by employing suitable boundary conditions.

In the rest of this paper, only variables with an overline are dimensional; unless specified otherwise, all variables are normalized by the water depth $\overline{h}$, fluid density $\overline{\rho}$, and the characteristic time scale $\sqrt{\overline{h}/\overline{g}}$, where $\overline{g}$ is the gravitational acceleration.

If we assume the fluid to be inviscid and incompressible and the flow irrotational, potential-flow theory can be applied. Using linearized free-surface boundary conditions, the total velocity potential Φ can be decomposed into the incident wave potential ϕ_0 associated with the undisturbed unit-amplitude incident wave, the diffraction potential ϕ_7,

Fig. 1 Problem schematic

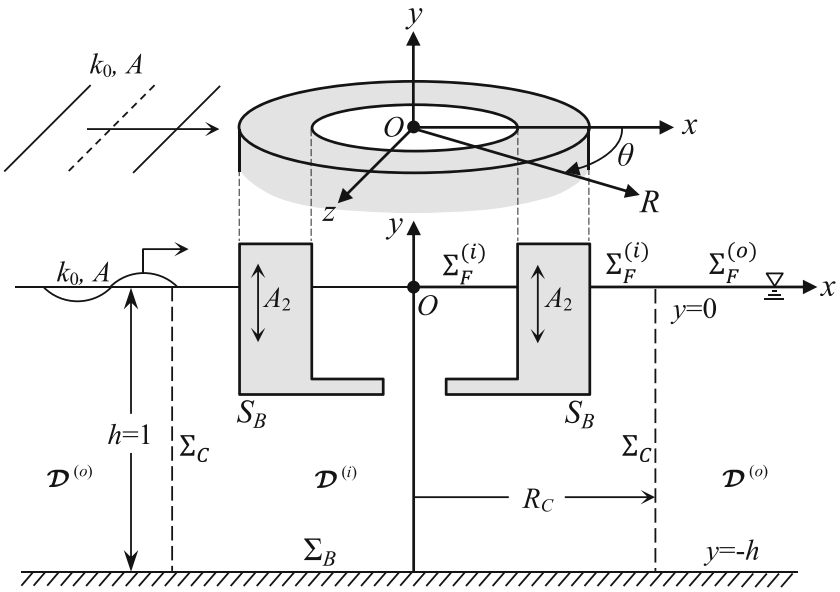

and the radiation potential ϕ_2 from the time-harmonic heave motion of the body:

$$\Phi = \Re\left\{A(\phi_0 + \phi_7)\mathrm{e}^{-\mathrm{i}\sigma t} + A_2(-\mathrm{i}\sigma)\phi_2\mathrm{e}^{-\mathrm{i}\sigma t}\right\} \tag{1}$$

where σ is the frequency of oscillation. The incident potential ϕ_0 of a linear wave propagating in the positive x-direction is known and given by

$$\phi_0 = -\frac{\mathrm{i}}{\sigma}\frac{\cosh k_0(y+1)}{\cosh(k_0)}\mathrm{e}^{\mathrm{i}k_0 x} \tag{2}$$

where $\mathrm{e}^{\mathrm{i}k_0 x}$ can be decomposed as

$$\mathrm{e}^{\mathrm{i}k_0 x} = \sum_{n=0}^{\infty} \mathrm{i}^n \epsilon_n J_n(k_0 R)\cos n\theta, \epsilon_n = \begin{cases} 1 \text{ if } n = 0 \\ 2 \text{ if } n \geq 1 \end{cases} \tag{3}$$

with J_n being the Bessel function of the first kind.

Inside the fluid domain $\mathcal{D}$, the radiation potential and the diffraction potential independently satisfy the Laplace's equation:

$$\nabla^2\phi_j = 0,\ j = 2, 7. \tag{4}$$

On the body surface S_B, the linearized boundary conditions of the radiation potential ϕ_2 and the diffraction potential ϕ_7 are given by

$$\left.\frac{\partial\phi_2}{\partial n}\right|_{S_B} = n_2 \tag{5}$$

$$\left.\frac{\partial\phi_7}{\partial n}\right|_{\mathcal{B}} = -\left.\frac{\partial\phi_0}{\partial n}\right|_{\mathcal{B}} \tag{6}$$

where n_2 is the y-component of the unit normal vector $\mathbf{n}$ of surface S_B pointing into the body. On the calm free surface Σ_F, the combined linearized free-surface boundary condition is applied:

$$\left[-\sigma^2\phi_j + \frac{\partial\phi_j}{\partial y}\right]_{y=0} = 0,\ j = 2, 7. \tag{7}$$

The no-penetration boundary condition is imposed on the bottom Σ_B:

$$\left.\frac{\partial\phi_j}{\partial y}\right|_{y=-h} = 0,\ j = 2, 7. \tag{8}$$

Finally, we have the far-field radiation condition requiring radially outgoing radiation and diffraction waves to decay faster than $1/\sqrt{R}$:

$$\lim_{k_0 R\to\infty}\left(\frac{\partial}{\partial R} - \mathrm{i}k_0\right)\left(\sqrt{R}\phi_j\right) = 0,\ j = 2, 7. \tag{9}$$

3 Hybrid Integral-Equation Method for Radiation and Diffraction Problems

The hybrid integral-equation method described in this section can be applied to a wide class of body geometries with a vertical axis of symmetry and arbitrary cross sections. Structures that are either surface-piercing or submerged, free-floating or bottom mounted can all be easily accommodated with trivial modifications to the algorithm. Furthermore, the current numerical method can also be used for multiple concentric bodies moving relative to each other, such as heaving point-absorber wave-energy converters. However, we shall restrict ourselves to the moonpool problem described in Section 2. At the end of the section, the computation of the radiation and wave excitation forces are briefly discussed. In particular, the wave force can be computed both directly by integrating

the scattered potential and indirectly from the radiation potential using reciprocity relations.

3.1 Formulation for the Inner Numerical Domain

Inside the inner numerical domain $\mathcal{D}^{(i)}$, the unit radiation potential ϕ_2 and the diffraction potential ϕ_7 are solved using the boundary element method. For a field point $P = (x, y, z) = (R, y, \theta)$ on the boundary of the inner domain $\partial\mathcal{D}^{(i)}$, we can write the following Fredholm integral equation of the second kind for solving the potentials ϕ_j with $j = 2, 7$ on the domain boundary:

$$2\pi\phi_j(P) = \iint_{\partial\mathcal{D}^{(i)}} \left[\frac{\partial\phi_j}{\partial\nu}(Q)G(P,Q) - \phi_j\frac{\partial G}{\partial\nu}\right] \mathrm{d}S(Q) \quad \text{if } P \in \partial\mathcal{D}^{(i)} \tag{10}$$

where $Q = (\xi, \eta, \zeta) = (\mathcal{R}, \eta, \vartheta)$ is the integration point and G is the Green's function. To differentiate from the normal vector $\mathbf{n}$ at P, the unit normal vector (pointing away from the domain) at Q is given by ν. Since we have a flat bottom, it is convenient to use the following Green's function with a simple source and its mirror image to automatically satisfy the bottom boundary condition on Σ_B (Lee 1985):

$$G(P,Q) = \frac{1}{r} + \frac{1}{r_1} \tag{11}$$

where

$$r = \sqrt{(x-\xi)^2 + (y-\eta)^2 + (z-\zeta)^2}$$
$$r_1 = \sqrt{(x-\xi)^2 + (y+\eta+2)^2 + (z-\zeta)^2}. \tag{12}$$

With the above choice of Green's function, the surface integral in Eq. 10 only needs to be carried out on the surfaces $S_B \cup \Sigma_F^{(i)} \cup \Sigma_C$.

Furthermore, by decomposing the velocity potentials into multiple circumferential modes, we can carry out the surface integral in the circumferential direction first (analytically when possible) to exploit the body symmetry about the y-axis for more efficient and accurate computation. With this approach, the full three-dimensional problem is decomposed into N independent "two-dimensional" problems to be solved in a plane of constant θ where N is the number of circumferential modes retained. For the radiation and diffraction potentials, we have:

$$\phi_j = \sum_{n=0}^{\infty} \varphi_j^n(R, y)\cos(n\theta),\ j = 2, 7. \tag{13}$$

Because of the body symmetry about the plane $z = 0$, only cosine circumferential modes are nonzero. In fact,only the axisymmetric mode of $n = 0$ is nonzero for the heave radiation potential with $\phi_2 = \varphi_2^0(R, y)$. With Eq. 13, Eq. 10 can be rewritten as

$$2\pi\varphi_j^n(R,y) = \int_{s^{(i)}} \frac{\mathcal{R}}{\sqrt{R}}\left[\frac{\partial\varphi_j^n}{\partial\nu} - \varphi_j^n\frac{\partial}{\partial\nu}\right]\frac{1}{\sqrt{\mathcal{R}}}C^n(R,y;\mathcal{R},\eta)\mathrm{d}s$$
$$\text{for } j = 2, 7,\ n = 0, 1, \ldots, \infty, \text{ and } (R,y) \in s^{(i)} \tag{14}$$

where

$$\sqrt{\frac{\mathcal{R}}{R}}C^n(R,y;\mathcal{R},\eta)\cos n\theta = \int_0^{2\pi}\cos n\vartheta\left(\frac{1}{r} + \frac{1}{r_1}\right)\mathcal{R}\,\mathrm{d}\vartheta. \tag{15}$$

The contour $s^{(i)}$ is the intersection between the vertical half plane of $\theta = 0$ and the surfaces Σ_C, $\Sigma_F^{(i)}$, and S_B. The differential area $\mathrm{d}S$ has been replaced by $\mathcal{R}\mathrm{d}\vartheta\mathrm{d}s$ where $\mathrm{d}s$ is the differential arc length element of the contour $s^{(i)}$.

It can be shown that C^n, which is related to the potential of a ring source (and its mirror image across the bottom) with strength varying as $\cos n\theta$, is given by the following expression:

$$C^n(R,y;\mathcal{R},\eta) = m_0 C_0^n + m_1 C_1^n \tag{16}$$

where

$$m_0^2 = \frac{4\mathcal{R}R}{(y-\eta)^2 + (\mathcal{R}+R)^2}$$
$$m_1^2 = \frac{4\mathcal{R}R}{(y+\eta+2)^2 + (\mathcal{R}+R)^2} \tag{17}$$

and

$$C_0^n = \int_{-\pi/2}^{\pi/2}\frac{\cos 2ne}{\sqrt{1 - m_0^2\cos^2 e}}\,\mathrm{d}e$$
$$C_1^n = \int_{-\pi/2}^{\pi/2}\frac{\cos 2ne}{\sqrt{1 - m_1^2\cos^2 e}}\,\mathrm{d}e. \tag{18}$$

For the special cases of $n = 0$ and $n = 1$, we have the following analytical expressions for C_0^n and C_1^n:

$$C_0^0 = 2K(m_0)$$
$$C_1^0 = 2K(m_1) \tag{19}$$

and (Lee 1985)

$$C_0^1 = \frac{4}{m_0^2}[K(m_0) - E(m_0)] - 2K(m_0)$$
$$C_1^1 = \frac{4}{m_1^2}[K(m_1) - E(m_1)] - 2K(m_1). \tag{20}$$

In the above equations, K and E are the Complete Elliptic Integrals of the first and second kind, respectively. Because heave radiation potential only involves the $n = 0$ mode, the analytical expressions in Eq. 19 allow very efficient computation of ϕ_2 since we only need to carry out numerical integration in the girth direction. Similarly, if we need the surge and pitch radiation potentials, which only involve the $n = 1$ mode, the expressions in Eq. 20 can be used. The computation of the diffraction potential is slightly more complicated because it potentially includes an infinite number of circumferential modes. In this case, Eq. 18 can be integrated numerically using, for example, a recursive adaptive quadrature to evaluate C_0^n and C_1^n for general non-negative integer values of n.

3.2 Formulation for the Outer Analytical Domain

In the outer analytical domain, the radiation and diffraction potentials can be represented using eigenfunctions which automatically satisfy the free-surface and bottom boundary conditions and the far-field radiation condition exactly:

$$\phi_j = \sum_{n=0}^{\infty} \left[\alpha_0^n \frac{H_n^{(1)}(k_0 R)}{|H_n^{(1)}(k_0 R_C)|} Y_0 + \sum_{i=1}^{\infty} \alpha_i^n \frac{K_n(k_i R)}{K_n(k_i R_C)} Y_i \right] \cos n\theta \tag{21}$$

where

$$Y_i(y) = \begin{cases} \cosh k_0(y+1)/\sqrt{N_0}, & \text{if } i = 0 \\ \cos k_i(y+1)/\sqrt{N_i}, & \text{if } i = 1, 2, \ldots \end{cases} \tag{22}$$

and

$$N_i = \begin{cases} \frac{1}{2}[1 + \sinh(2k_0)/2k_0], & \text{if } i = 0 \\ \frac{1}{2}[1 + \sin(2k_i)/2k_i], & \text{if } i = 1, 2, \ldots \end{cases} \tag{23}$$

In the above equations, $H_n^{(1)}$ is the Hankel function of the first kind and K_n is the modified Bessel function of the second kind. The normalization factors of $|H_n^{(1)}(k_0 R_C)|$ and $K_n(k_i R_C)$ are included so that the unknown constant coefficients α_0^n and α_i^n are suitably scaled for arbitrary choice of R_C. The values of k_0 and k_i are given by the dispersion relations:

$$\begin{aligned} \sigma^2 &= k_0 \tanh(k_0) \\ \sigma^2 &= k_i \tan(k_i) \text{ for } i = 1, 2, \ldots \end{aligned} \tag{24}$$

Again, only cosine circumferential modes need to be retained because of the symmetry.

3.3 Numerical Procedure

In the inner domain, Eq. 14 is solved numerically by discretizing the contour $s^{(i)}$ into a sequence of N_T linear panels $s_j^{(i)}$ where $j = 1, 2, \ldots, N_T$ as shown in Fig. 2. The panels are numbered in the counterclockwise direction with panels $s_1^{(i)}$ to $s_{N_C}^{(i)}$ covering the matching boundary s_C. The portion of the free surface s_F external to the body is represented by panels $s_{N_C+1}^{(i)}$ to $s_{N_2}^{(i)}$. The submerged portion of the body s_B consists of panels $s_{N_2+1}^{(i)}$ to $s_{N_3}^{(i)}$. Finally, the internal moonpool section of the free surface s_F is discretized into panels $s_{N_3+1}^{(i)}$ to $s_{N_T}^{(i)}$.

Each circumferential mode of the diffraction potential φ_7^n and the heave radiation potential $\phi_2 = \varphi_2^0$ can be solved independently following the same procedure apart from the different boundary conditions on s_B. Therefore, in this section, we shall simply use φ^n to represent the unknown potential component and reserve the subscript for the panel number. The values of φ^n and $\partial\varphi^n/\partial\nu$ are assumed to be constant on each panel with $\varphi^n = \varphi_j^n$ and $\partial\varphi^n/\partial\nu = (\partial\varphi^n/\partial\nu)_j$ on $s_j^{(i)}$. The constant panel approximation used here is found to be adequately fast and accurate. The field point P is placed at the midpoint of the i-th panel (R_i, y_i).

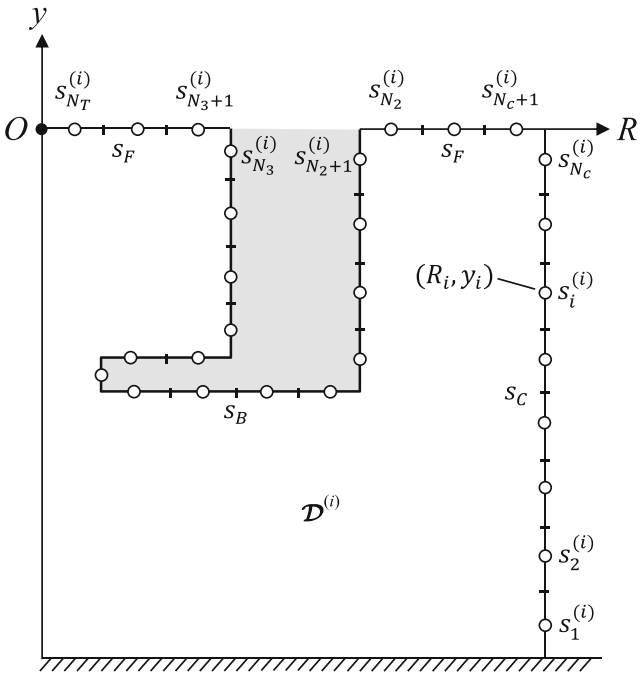

Fig. 2 Discrete representation of contour $s^{(i)} = s_C \cup s_F \cup s_B$.The contours s_C, s_F, and s_B are the intersections between the half plane of $\theta = 0$ and Σ_C, $\Sigma_F^{(i)}$, and S_B, respectively

With the above assumptions and the free-surface boundary condition given in Eq. 7, Eq. 14 can be put into the following discrete form:

$$
\begin{aligned}
&2\pi\varphi_i^n - \sum_{j=1}^{N_C} M_{ij}\left(\frac{\partial\varphi^n}{\partial\mathcal{R}}\right)_j + \sum_{j=1}^{N_C} N_{ij}\varphi_j^n \\
&+ \sum_{j=N_C+1}^{N_2} (N_{ij} - \sigma^2 M_{ij})\varphi_j^n + \sum_{j=N_2+1}^{N_3} N_{ij}\varphi_j^n \\
&+ \sum_{j=N_3+1}^{N_T} (N_{ij} - \sigma^2 M_{ij})\varphi_j^n \\
&= \sum_{j=N_2+1}^{N_3} M_{ij}\left(\frac{\partial\varphi^n}{\partial\nu}\right)_j
\end{aligned}
\tag{25}
$$

where $i = 1, 2, \ldots, N_T$ and

$$
\begin{aligned}
M_{ij} &= \int_{s_j^{(i)}} \sqrt{\mathcal{R}/R_i}\, C^n(R_i, y_i; \mathcal{R}, \eta)\, \mathrm{d}s \\
N_{ij} &= \int_{s_j^{(i)}} \frac{\mathcal{R}}{\sqrt{R_i}} \frac{\partial}{\partial\nu}\left(\frac{C^n}{\sqrt{\mathcal{R}}}\right) \mathrm{d}s
\end{aligned}
\tag{26}
$$

The function C^n is given by Eq. 16. The integration over each linear panel in Eq. 26 is carried out numerically using the five-point Gauss-Legendre quadrature if the field point P is not on the panel. If P is on $s_j^{(i)}$, the function C^n has a logarithmic singularity. In this case, the integration over a small region near the singular point occupied by P is carried out analytically with the remaining parts of the panel on each side of the singular point integrated using the five-point quadrature as usual.

Finally, to close the system of equations given in Eq. 25, the continuity of the velocity potential and its normal derivative across the matching boundary $R = R_C$ needs to be enforced with the help of the analytical eigenfunction solution in the external flow domain $\mathcal{D}^{(o)}$. From Eq. 21, the radiation potentials and their normal derivatives on the matching shell can be expressed in terms of the constant coefficients α_j^n's:

$$
\phi_i = \sum_{j=0}^{\infty} A_{ij}\alpha_j^n \text{ and } \left(\frac{\partial\phi}{\partial R}\right)_i = \sum_{j=0}^{\infty} B_{ij}\alpha_j^n
\tag{27}
$$

where

$$
A_{ij} = \begin{cases} \dfrac{H_n^{(1)}(k_0 R_C)}{|H_n^{(1)}(k_0 R_C)|} Y_0(y_i) & \text{if } j = 0 \\ Y_j(y_i) & \text{if } j = 1, 2, \ldots \end{cases}
\tag{28}
$$

and

$$
B_{ij} = \begin{cases} k_0 \dfrac{H_n^{(1)'}(k_0 R_C)}{|H_n^{(1)}(k_0 R_C)|} Y_0(y_i) & \text{if } j = 0 \\ k_j \dfrac{K_n'(k_j R_C)}{K_n(k_j R_C)} Y_j(y_i) & \text{if } j = 1, 2, \ldots \end{cases}
\tag{29}
$$

For implementation, the infinite sums in Eq. 27 need to be truncated. For convenience, we shall only keep the first N_C terms to match the number of panels we have on the matching boundary.

With Eq. 27, we can rewrite Eq. 25 into the following form:

$$
\begin{aligned}
&2\pi\varphi_i^n + \sum_{j=1}^{N_C}\left[N_{ij} - (MBA^{-1})_{ij}\right]\varphi_j^n \\
&+ \sum_{j=N_C+1}^{N_2} (N_{ij} - \sigma^2 M_{ij})\varphi_j^n + \sum_{j=N_2+1}^{N_3} N_{ij}\varphi_j^n \\
&+ \sum_{j=N_3+1}^{N_T} (N_{ij} - \sigma^2 M_{ij})\varphi_j^n \\
&= \sum_{j=N_2+1}^{N_3} M_{ij}\left(\frac{\partial\varphi^n}{\partial\nu}\right)_j
\end{aligned}
\tag{30}
$$

The right-hand side is known from the boundary conditions on the body surface. More specifically, the body boundary condition of $\phi_2 = \varphi_2^0$ is given by Eq. 5 while the boundary condition for the diffraction potential component φ_7^n can be constructed from Eqs. 2 and 6 with the help of the ring-wave decomposition given in Eq. 3. Equation 30 is a well-posed problem and can be easily solved for the unknown potentials on the contour $s^{(i)}$.

3.4 Radiation and Wave Excitation Forces

The radiation force associated with the body heave motion is given in terms of the heave added masses and wave damping coefficients. The non-dimensional added mass and damping coefficient are given by:

$$
\mu_{22} + \mathrm{i}\lambda_{22} = \frac{\overline{\mu}_{22} + \mathrm{i}\frac{\overline{\lambda}_{22}}{\overline{\sigma}}}{\pi\overline{\rho}\,\overline{a}^3} = \frac{2}{a^3}\int_{s_B} \phi_2 R n_2\, \mathrm{d}s
\tag{31}
$$

where $a = \overline{a}/\overline{h}$ is the characteristic radius of the body.

There are two ways to obtain the complex heave wave excitation force. First, we can directly integrate the scattered potential $\phi_s = \phi_0 + \phi_7$ on the body surface:

$$
X_2 = \frac{\overline{X}_2}{\pi\overline{\rho}\,\overline{g}\,\overline{a}^2} = \frac{\mathrm{i}\sigma}{\pi a^2}\iint_{S_B} \phi_s n_2\, \mathrm{d}S
\tag{32}
$$

where X_2 is the complex amplitude of the wave force in heave per unit incident wave amplitude. In fact, only the axisymmetric $n = 0$ mode of the scattered potential has a nonzero contribution to X_2, and there is no need to compute the higher-order circumferential modes of ϕ_7 if only the heave force is of interest.

Alternatively, X_2 can be obtained indirectly from the far-field heave radiation potential (Wehausen 1971; Wehausen et al. 2016) using the Haskind relation (Haskind 1957).

$$X_2 = -\frac{4i\alpha_0^0\sqrt{N_0}}{\pi a^2 \cosh(k_0)|H_n^{(1)}(k_0 R_C)|} \tag{33}$$

The complex constant coefficient α_0^0 comes from the outer analytical solution of ϕ_2. These coefficients can be determined from Eq. 27 once the radiation potential on the matching boundary R_C is solved. Similar expressions also exist for the wave excitation force and moment in the surge and pitch directions (Yeung 1981; Bachynski et al. 2012). This indirect approach completely removes the need to solve for the diffraction potential when determining the wave excitation forces and moments. Nevertheless, it can still be beneficial to solve for the diffraction potential if information on the wave field is needed or as a numerical check since the wave forces and moments computed using the two methods should closely agree with each other.

4 Numerical Results

The hybrid integral-equation method is applied to investigate the hydrodynamic properties of two different axisymmetric structures with a moonpool: a thick-walled moonpool with a bottom plate that restricts opening and a spar-like structure with a diverging bottom opening. The latter geometry in particular involves sloped walls that make the method of matched eigenfunctions very tedious to apply but can be effortlessly accommodated using the current hybrid method.

4.1 Thick-Walled Moonpool with Bottom Plate

The body geometry being considered in this section is illustrated in Fig. 3. The moonpool wall has a draft of d and an outer radius of a which is taken as the characteristic body radius for computing μ_{22}, λ_{22}, and X_2 as defined in Eqs. 31 and 32. The moonpool radius and depth (measured to the top of the bottom plate) are a_1 and d_1, respectively. The bottom plate has a center opening of radius a_0 ($a_0 \le a_1$). For all subsequent results, both s_C and s_F are discretized into 100 panels. On the body surface, we have used a panel size of 0.002. The radius of the matching boundary is set to $R_C = 1.5a$. The exact choice of R_C does not impact the results as long as enough panels are used to properly resolve the free surface of the inner numerical domain.

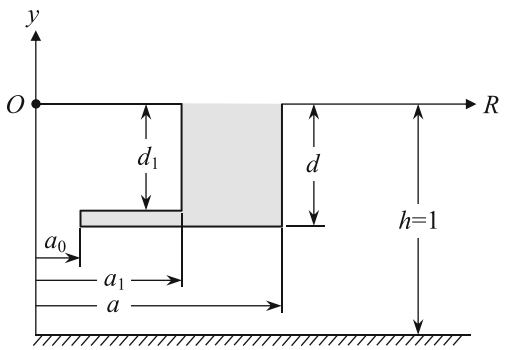

Fig. 3 Cross section of a thick-walled moonpool with bottom plate in a vertical plane of constant θ

The effects of the opening size a_0 on the moonpool behavior and the hydrodynamic properties of the structure are of primary interest. However, as a validation, we shall first consider two cases with no bottom plate, i.e. $a_0/a_1 = 1$, and different wall thickness. The geometric parameters are $d = 1/6$, $a_1 = 0.5$, and $a = 0.6$ or 0.9. The computed heave added mass, wave damping coefficient, and the magnitude of wave excitation force in heave are shown in Fig. 4. The added mass and damping coefficient computed using the method of matched eigenfunctions (Mavrakos 1988) are also included for comparison, showing good agreement with the current results. Furthermore, the wave forces computed both directly from the scattered potential and indirectly from the radiation potential are consistent with each other as shown in Fig. 4c, further validating the current method.

The first zero-damping frequency, associated with the Helmholtz (pumping) mode of moonpool resonance, is observed at approximately $\overline{\sigma}^2\overline{a_1}/\overline{g} = 1.22$ and 1.47 for $a = 0.9$ and 0.6, respectively. Two higher-order resonance modes of the moonpool are found at around $\overline{\sigma}^2\overline{a_1}/\overline{g} = 3.88$ and 7.03 for both geometries. At these frequencies, added mass and damping coefficient show prominent spikes with added mass switching sign across the resonance frequency. These higher-order resonance modes, which are associated with standing waves inside the moonpool, are primarily influenced by the moonpool radius, which is the same for both geometries, and the wall thickness has little influence on the locations of the higher-order modes. At these resonance frequencies, the amplitudes of the radiated waves inside the moonpool are unrealistically large because of a lack of viscous damping; however, the overall shape of the free-surface elevation $\overline{\eta}(\overline{R}, \theta, \overline{t})$ inside the moonpool is still of significant practical interest. The moonpool wave fields computed from the heave radiation potential are shown in Fig. 5 near the Helmholtz mode and the first two higher-order modes for the case of $a = 0.6$. For the first and second higher-order resonances shown in Figs. 5b and c, about half and one period of standing wave fit in the radial direction inside the moonpool, respectively. This behavior is essentially the three-dimensional axisymmetric analogy of what is observed in a two-dimensional moonpool between two infinitely long cylinders (Yeung and Seah 2007).

Next, a bottom plate with thickness $(d - d_1)/d = 0.05$ is added to the thick-walled moonpool with draft $d = 1/6$

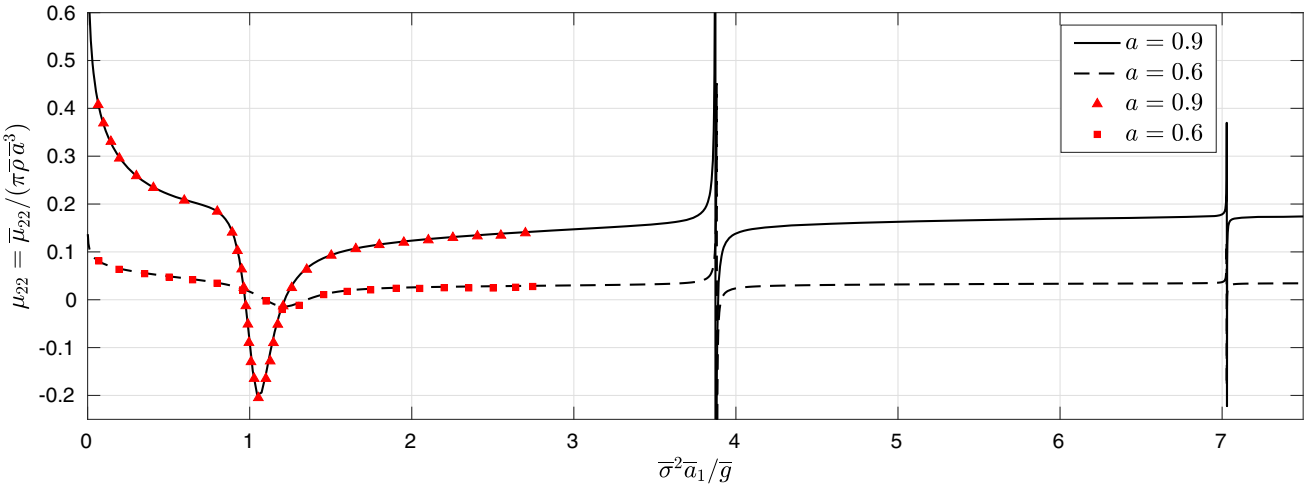

(a) Heave added mass.

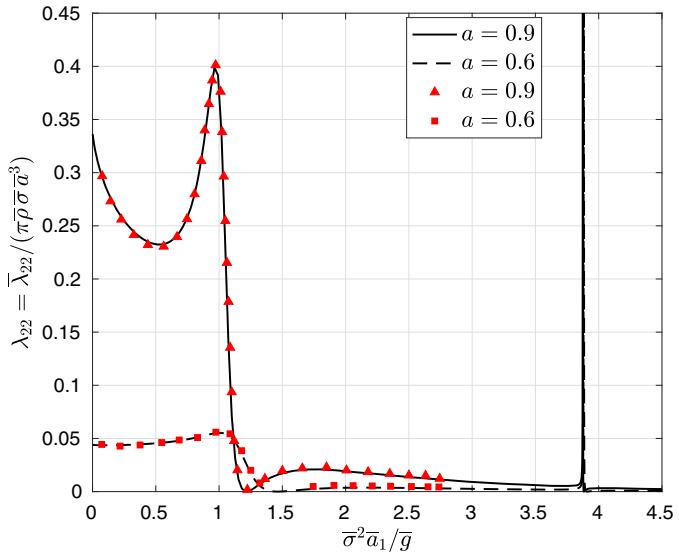

(b) Wave damping coefficient.

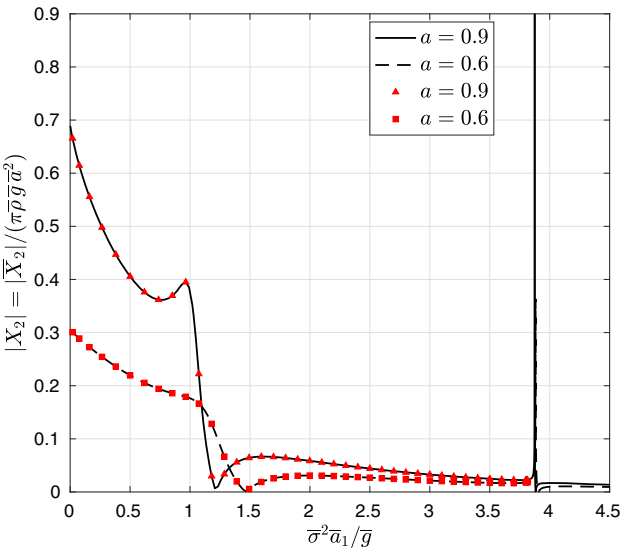

(c) Magnitude of wave excitation force.

Fig. 4 Heave added mass (**a**), wave damping coefficient (**b**), and the magnitude of wave excitation force in heave (**c**) of a thick-walled moonpool with no bottom plate ($a_0/a_1 = 1$). $d = 1/6$, $a_1 = 0.5$, and $a = 0.6$ and 0.9. In (**a**) and (**b**), the curves are results from the current hybrid integral-equation method, and the symbols are solutions of the matched eigenfunction method by Mavrakos (1988). In (**c**), the curves represent wave force computed indirectly from the heave radiation potential while the symbols are obtained through direct integration of the scattered potential

and outer and inner radii of $a = 0.9$ and $a_1 = 0.5$, respectively. The opening size of the bottom plate is varied from $a_0/a_1 = 0.2$ to 1.0. The computed heave added mass, damping coefficient, and wave excitation force are shown in Fig. 6a–c. For comparison, the hydrodynamic coefficients of a simple truncated cylinder with the same draft and outer radius as the moonpool are also included (labeled $a_0/a_1 = 0$). Several interesting observations can be made. First, the zero-damping frequency associated with the pumping-mode resonance increases with the opening size of the bottom plate. As a_0 decreases, a progressively more prominent peak in heave added mass develops at a frequency slightly higher than the pumping-mode zero-damping frequency (see Fig. 6a). Furthermore, no negative added mass is observed with intermediate opening sizes of $a_0/a_1 = 0.4$ to 0.8 for the range of frequencies shown. Negative added mass is only observed at the two extremes of no bottom plate $a_0/a_1 = 1.0$ and very small opening size of $a_0/a_1 = 0.2$. Away from the moonpool resonance, heave added mass increases with decreasing opening size as expected. In Fig. 6b, the peak in damping preceding (at a lower frequency) the zero-damping frequency of the pumping-mode resonance diminishes as the bottom-plate opening size decreases while a prominent spike in damping

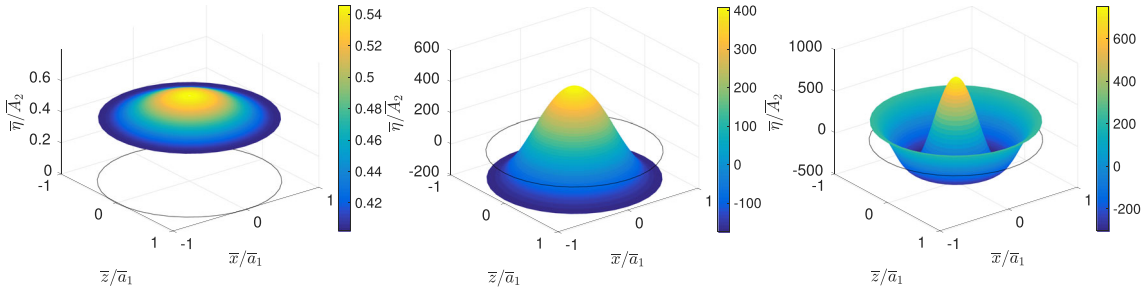

(a) Pumping-mode resonance. (b) First higher-order resonance. (c) Second higher-order resonance.

Fig. 5 Free-surface elevation (normalized by the amplitude of body heave motion) inside the moonpool at the time instant with maximum wave elevation at the center ($\overline{R} = 0$). Panels (**a**), (**b**), and (**c**) are obtained near the zero-damping frequencies associated with the pumping-mode resonance and the first and second higher-order resonances, respectively. The dark circle represents the calm waterline inside the moonpool. $a_0/a_1 = 1$, $d = 1/6$, $a_1 = 0.5$, and $a = 0.6$

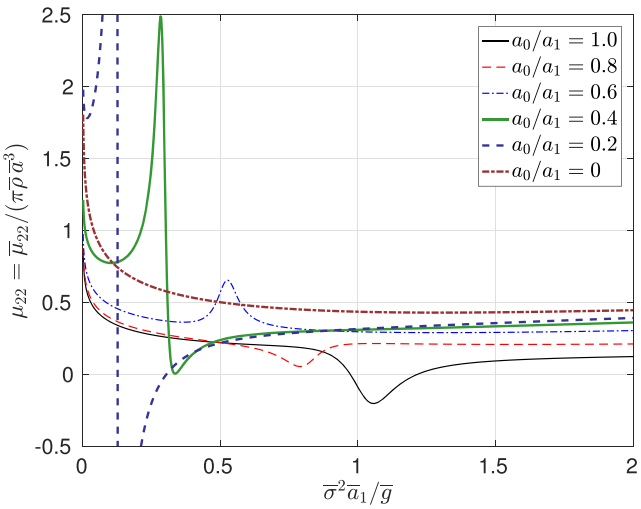

(a) Heave added mass.

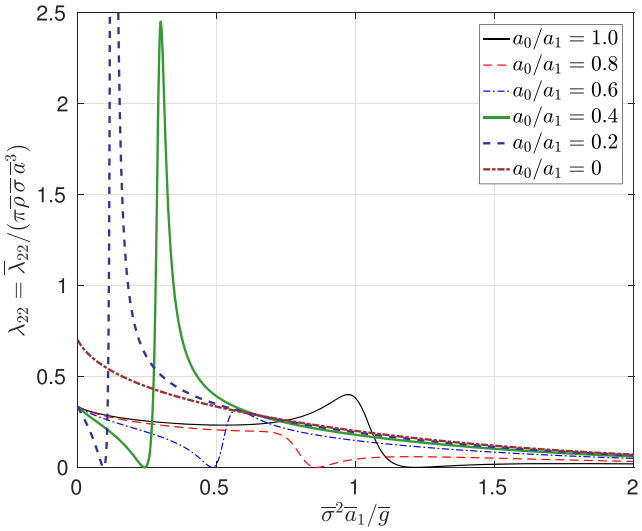

(b) Damping coefficient.

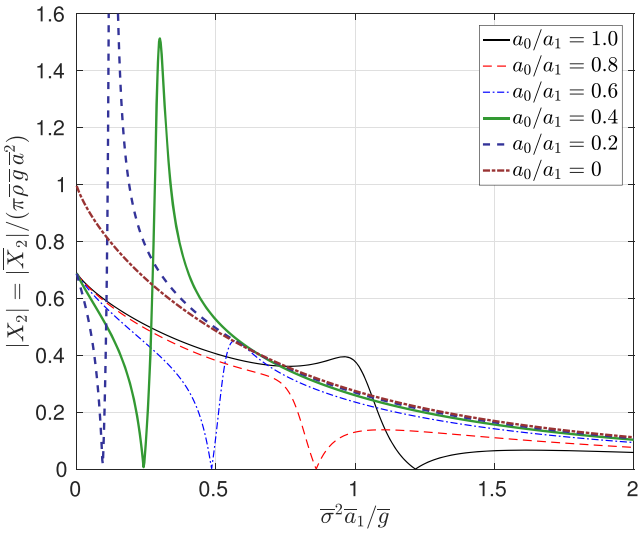

(c) Magnitude of wave excitation force.

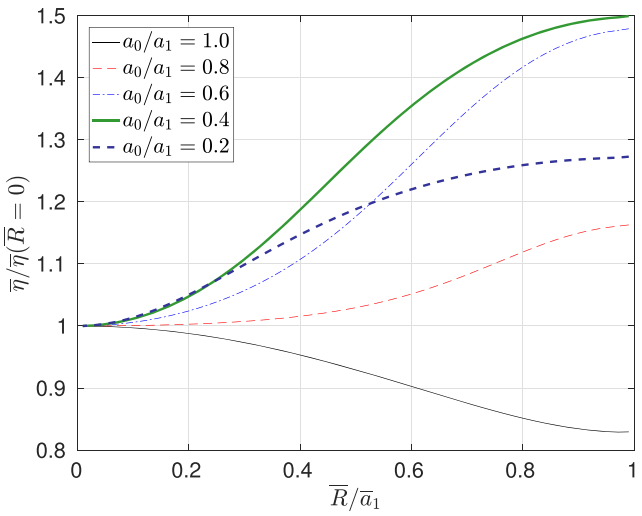

(d) Shape of moonpool free surface.

Fig. 6 Heave added mass (**a**), damping coefficient (**b**), the magnitude of the wave excitation force in heave (**c**), and the normalized shape of the moonpool free surface, at the time instant of maximum wave elevation at the moonpool center ($\overline{R} = 0$), obtained near the zero-damping frequency associated with the pumping-mode resonance (**d**). $(d - d_1)/d = 0.05$, $d = 1/6$, $a_1 = 0.5$, and $a = 0.9$

develops right after the zero-damping frequency. The spikes in damping are located at slightly higher frequencies than the spikes in added mass. The magnitude of the wave force follows a similar trend as the damping coefficient (see Fig. 6c). As the frequency approaches zeros, the wave excitation forces in heave all approach 0.69 which is the ratio of the waterplane area of the moonpool wall to that of a simple truncated cylinder with the same outer radius.

The shapes of the free surface in the moonpool near the zero-damping frequency of pumping-mode resonance are computed from the radiation potential and compared in Fig. 6d. Interestingly, even for very large openings of the bottom plate, the cross section of the moonpool free surface "flips" with maximum wave amplitude occurring at the wall of the moonpool instead of the center as in the case with no bottom plate. Maximum variation of the moonpool wave amplitude with radius is observed for the intermediate opening size of $a_0/a_1 = 0.4$. Near the zero-damping frequency of pumping-mode resonance, the oscillation of the moonpool free surface and the body heave motion are always out-of-phase by approximately one-half period for all opening sizes; as the structure moves downward, part of the water displaced by the structure enters the moonpool through the opening of the bottom plate, leading to a net increase of free-surface elevation inside the moonpool. This means that, as far as inviscid fluid is concerned, the flow will never approach that with a completely closed bottom plate, which requires moonpool free-surface oscillation to be in phase with the body motion at all times, no matter how small the bottom opening size a_0 becomes. This may partially explain the emergence of a spike in heave added mass near the pumping-mode resonance frequency for small bottom opening radius a_0: water needs to rapidly accelerate to enter or exit the moonpool through the small opening at high speed, thus increasing the added mass experienced by the structure.

4.2 Spar with Diverging Bottom Opening

A spar-shaped body with a moonpool and a diverging bottom opening shown in Fig. 7 is investigated. This particular geometry is inspired by designs of floating OWCs (Falcão et al. 2012).

As shown in Fig. 7a, the outer surface of the spar has two sloped sections at the top and bottom connected by a vertical section of radius a_1 in the middle; the inner surface facing the moonpool consists of only a vertical section and a sloped section at the bottom. The gap between the inner and outer surfaces at the bottom edge is closed by a semicircular cap of diameter $\delta = a_1 - a_0$ which is the thickness of the moonpool wall. The radius and draft at the lower end of the outer surface is a_2 and d, respectively. The radius of the moonpool is a_0. To investigate the effect of the diverging bottom opening, the value of a_2 is increased from a_1 (i.e. vertical wall) to a, the outer radius of the structure at the calm waterline, while all the other geometric parameters are fixed with $a = 1/6$, $a_0 = 1/30$, $a_1 = 1/20$, and $d = 1/2$. The moonpool is considered to be open to the air, and we will not attempt to model the effects of the air chamber and turbine above the moonpool as in an actual OWC which is beyond the scope of the current paper. Furthermore, the narrowness of the moonpool means that, in the range

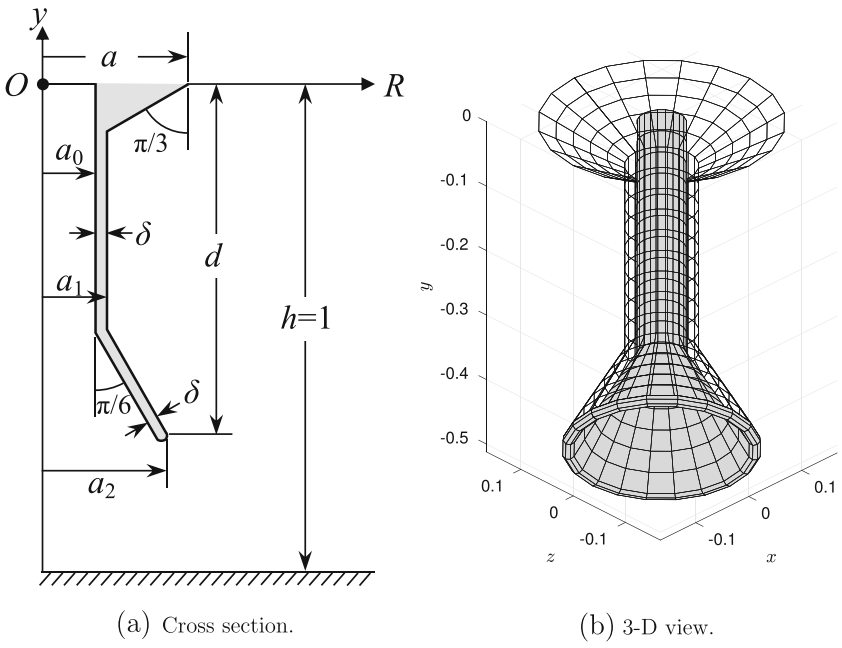

(a) Cross section. (b) 3-D view.

Fig. 7 Geometry of an OWC-inspired spar with moonpool. **a** Cross section of the spar in a plane of constant θ. **b** Three-dimensional view of the wetted surface of the spar with the inner surface and the rounded bottom edge in light gray and the outer surface transparent

of frequency of practical interest, only the pumping-mode resonance will be encountered. All results shown in this section are computed using a non-dimensional panel size of 0.01. The matching boundary and the inner-domain free surface (moonpool free surface included) both consist of 100 panels. The radius of the matching boundary is chosen to be $R_C = 1.5a$.

The hydrodynamic properties are shown in Fig. 8 for several different values of a_2. As a_2 increases, the frequency of zero damping increases, following the same trend observed in Section 4.1 where the zero-damping frequency associated with the pumping-mode resonance increases with the radius of the bottom-plate opening.

As shown in Fig. 8a, the heave added mass of the spar when $a_2/a_1 = 1$ is similar to that of a thick-walled moonpool with no bottom plate shown in Fig. 4a. A trough in heave added mass is observed slightly before the pumping-mode zero-damping frequency. However, for the current spar geometry, the trough is extremely narrow-banded as a consequence of the narrowness of the moonpool relative to the wavelength. As a_2/a_1 increases, a progressively more prominent positive spike followed by a negative one in heave added mass develops. Again, the negative spike is located at a frequency slightly lower than the pumping-mode zero-damping frequency. The bandwidths of the peak and trough also increase

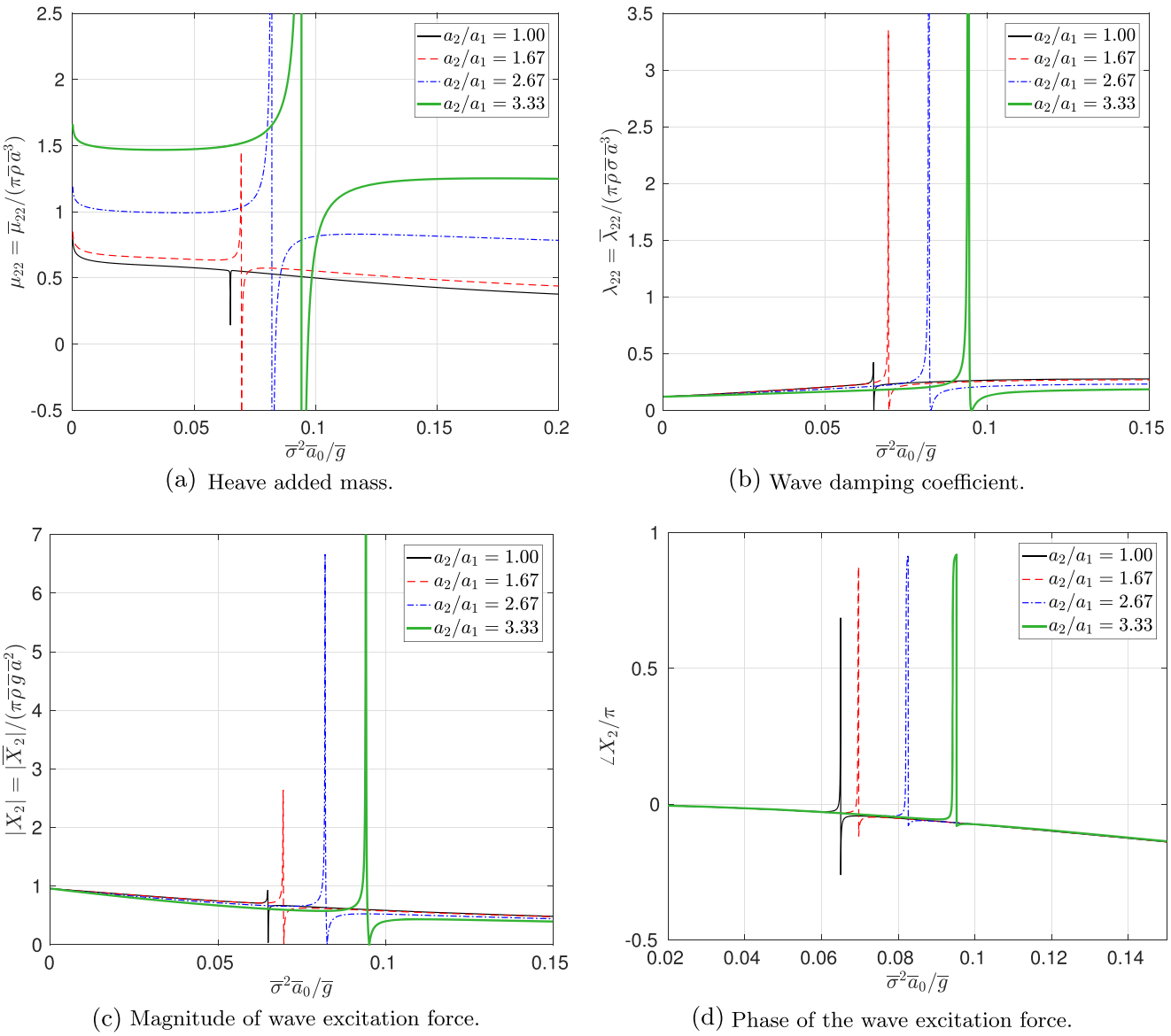

(a) Heave added mass.

(b) Wave damping coefficient.

(c) Magnitude of wave excitation force.

(d) Phase of the wave excitation force.

Fig. 8 Heave added mass (**a**), wave damping coefficient (**b**), and the magnitude (**c**) and phase (**d**) of the wave excitation force in heave of a spar-like structure with moonpool. $a = 1/6$, $a_0 = 1/30$, $a_1 = 1/20$, and $d = 1/2$. The wave excitation forces are computed indirectly from the heave radiation potential

slightly with a_2. Away from the moonpool resonance frequency, the heave added mass increases with the size of the bottom opening as expected which should lead to a lower heave resonance frequency of the spar itself.

In Fig. 8b, a spike in damping is observed at a frequency slightly lower than that of zero damping, and the magnitude of the spike increases rapidly with increasing a_2. Interestingly, this is the opposite of the observation made in Section 4.1 where a spike in damping develops at a frequency slightly higher than the pumping-mode zero-damping frequency when the opening is being restricted by the bottom plate. Furthermore, a larger bottom opening surprisingly results in lower wave damping coefficient away from the moonpool resonance frequency. The magnitude of the wave excitation force follows approximately the same trend as that of the damping coefficient.

The phase of the wave force given in Fig. 8d shows interesting behaviors. The phase of X_2 increases rapidly but smoothly at a frequency slightly lower than the zero-damping frequency. The halfway point of this phase shift roughly aligns with the spike in damping shown in Fig. 8b. At the frequency of zero damping, however, the phase of X_2 jumps back discontinuously by approximately one half period, canceling the previous phase shift. Away from the resonance frequency, the phase of X_2 is the same for all four geometries.

If the spar is allowed to heave (one degree of freedom) with complex amplitude A_2 under the excitation of a regular incident wave with potential given by Eq. 2, the Response Amplitude Operator (RAO_2) of the body can be computed using the following equation:

$$\mathrm{RAO}_2 = \frac{\overline{A}_2}{\overline{A}} = \frac{\overline{X}_2}{-(\overline{m}+\overline{\mu}_{22})\overline{\sigma}^2 + \overline{K}_{22} - \mathrm{i}\overline{\lambda}_{22}\overline{\sigma}} \tag{34}$$

where $\overline{m}$ and $\overline{K}_{22} = \pi\overline{\rho}\,\overline{g}(\overline{a}^2 - \overline{a}_0^2)$ are the mass and hydrostatic spring constant of the spar structure. The free

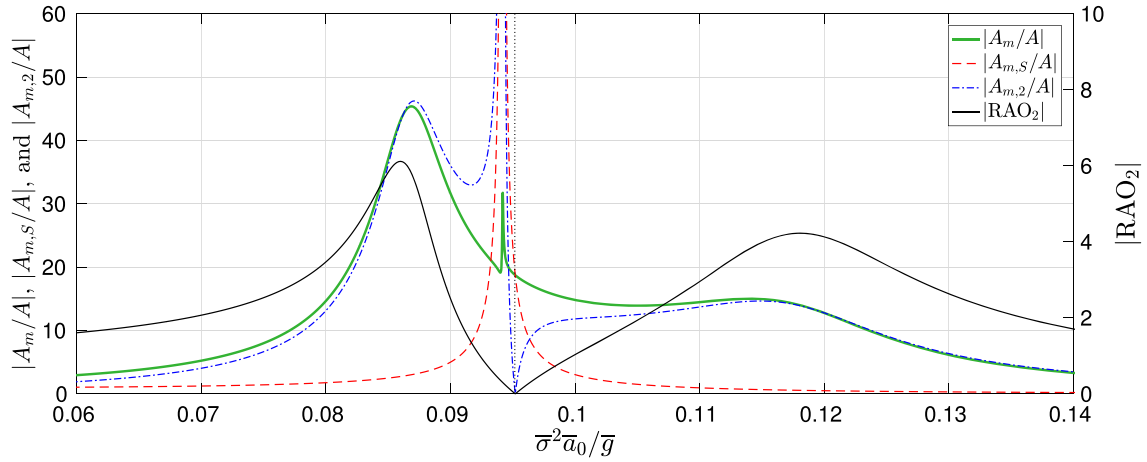

(a) Magnitudes.

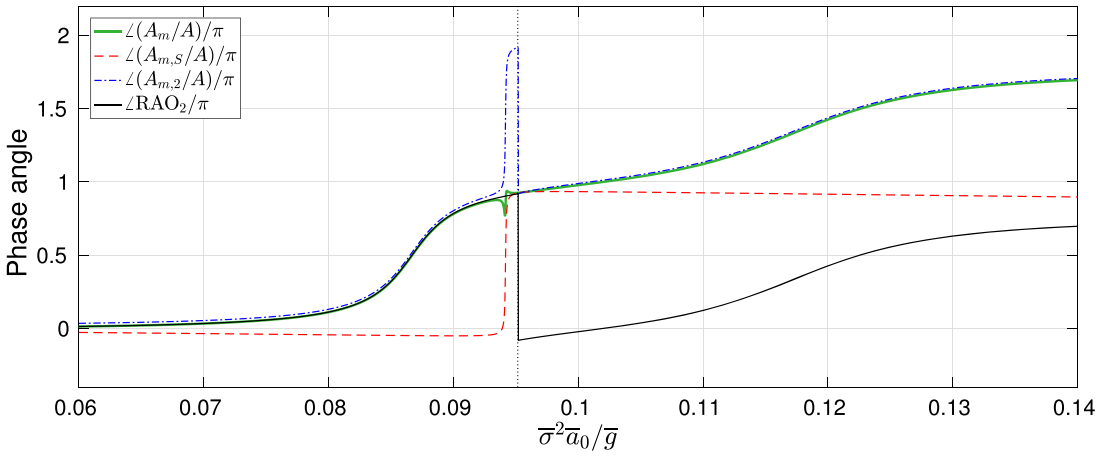

(b) Phases.

Fig. 9 The magnitudes (**a**) and phases (**b**) of the spatially averaged moonpool wave amplitude and heave RAO of the spar. $a = 1/6$, $a_0 = 1/30$, $a_1 = 1/20$, $a_2 = a$ and $d = 1/2$

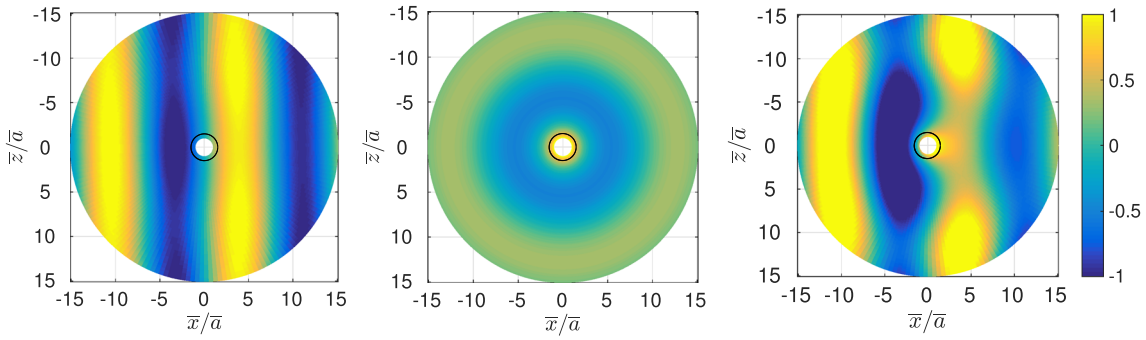

(a) Scattered wavefield. (b) Radiated wavefield. (c) Total wavefield.

Fig. 10 Wave fields near the spar at the time instant of maximum positive moonpool free-surface elevation. $\overline{\sigma}^2\overline{a}_2/\overline{g} = 0.087$ (near heave resonance of the spar), $a = 1/6$, $a_0 = 1/30$, $a_1 = 1/20$, $a_2 = a$ and $d = 1/2$. The scattered, radiated, and total wave elevations, normalized by the incident wave amplitude, are shown in (**a**), (**b**), and (**c**), respectively

surface of the moonpool remains approximately flat because of the small radius of the moonpool relative to the wave length. Therefore, the motion of the internal free surface can be effectively represented using a complex amplitude $A_m = A_{m,S} + A_{m,2}$ averaged over the moonpool area. The two components $A_{m,S}$ and $A_{m,2}$ are contributions from the scattered waves and the radiated waves from body heave motion, respectively. To further investigate the behavior of the moonpool free surface and the body motion, the values of RAO_2, A_m/A, $A_{m,S}/A$, and $A_{m,2}/A$ are all computed and shown in Fig. 9 for the case with $a = 1/6$, $a_0 = 1/30$, $a_1 = 1/20$, $a_2 = a$ and $d = 1/2$.

Heave resonance of the spar occurs at $\overline{\sigma}^2\overline{a}_0/\overline{g} = 0.086$, lower than the zero-damping frequency associated with moonpool resonance at 0.095 (see Fig. 9a). At the zero-damping frequency, the magnitude of RAO_2 is zero because of zero wave force. The contribution to moonpool wave from the scattered potential, $|A_{m,S}/A|$, shows a spike at a frequency slightly lower than the zero-damping frequency. A spike in $|A_{m,2}/A|$ is also observed at the same frequency. Away from this point, $|A_{m,2}/A|$ more or less follows the same trend as $|\mathrm{RAO}_2|$ with a zero at the zero-damping frequency. Interestingly, around the spikes in $|A_{m,S}/A|$ and $|A_{m,2}/A|$, both $A_{m,S}$ and $A_{m,2}$ undergo a rapid but smooth increase in phase while approximately stay out-of-phase by one-half period from each other (see Fig. 9b). As a result, the contributions from scattered waves and radiated waves roughly cancel each other, and a more moderate spike is observed at this frequency in the total moonpool wave amplitude $|A_m/A|$. The highest moonpool wave amplitude is, in fact, observed at the heave resonance frequency of the spar with the scattered waves having negligible contribution to the pumping motion of the moonpool free surface.

Finally, the wave fields near the spar at the time instant of maximum positive moonpool free-surface elevation are shown in Fig. 10. The spar is experiencing heave resonance with $\overline{\sigma}^2\overline{a}_0/\overline{g} = 0.087$ which leads to maximum moonpool wave amplitude. The blank area in the center is occupied by the spar. The moonpool free-surface is not shown because it is effectively flat. The dark circle surrounding the blank area marks the matching boundary between in the inner and outer domains used in the computation. Good solution matching between the two domains is achieved as indicated by the smooth wave fields at the domain boundary.

5 Conclusions

An efficient and robust hybrid integral-equation method for solving the wave radiation and diffraction problems about axisymmetric bodies of arbitrary cross sections is presented. The method utilizes an analytical eigenfunction representation of the velocity potential in the semi-infinite outer domain and a "two-dimensional" boundary element method in the numerical inner domain containing the body. Ring sources and dipoles are utilized to exploit the body symmetry for more efficient computation, and the continuity of flux and pressure is enforced on the matching boundary between the two domains.

The solutions of the hybrid method are first validated through comparison with existing results for a thick-walled moonpool computed using the method of matched eigenfunctions. Subsequently, the hybrid method is applied to two different axisymmetric bodies with a circular moonpool that are of significant practical interest: a thick-walled moonpool with a bottom plate the restricts the opening and a spar-like structure with a diverging bottom opening inspired by designs of floating Oscillating Water Columns (OWCs). For both geometries, the effects of the size of the bottom opening on the hydrodynamic properties of the structures are investigated. In particular, it is discovered that, for both geometries, the zero-damping frequency associated with the Helmholtz (pumping-mode) resonance of the moonpool generally increases with

increasing radius of the bottom opening. For the thick-walled moonpool with bottom plate, the shape of the moonpool free surface near the pumping-mode zero-damping frequency is investigated. It is observed that the bottom plate, even with relatively large opening, tends to cause the moonpool free surface to "flip" with maximum amplitude observed at the moonpool wall instead of the center as is the case with no bottom plate. Finally, the motion of the OWC-inspired spar-like structure is computed by allowing it to heave freely under the excitation of regular incident waves. Both the radiation and scattered components lead to significant moonpool motion at a frequency slightly below the pumping-mode zero-damping frequency. However, the two contributions are out-of-phase by one-half period from each other, potentially resulting in significant cancellation and a more moderate total moonpool wave amplitude. The strongest moonpool motion is, in fact, observed at the heave resonance frequency of the structure itself with negligible contribution from the scattered waves.

Acknowledgments Partial support for this work was provided by the American Bureau of Shipping Endowed Chair in Ocean Engineering held by the first author.

References

Bachynski EE, Young YL, Yeung RW (2012) Analysis and optimization of a tethered wave energy converter in irregular waves. Renew Energy 48:133–145. https://doi.org/10.1016/j.renene.2012.04.044

Chau FP, Yeung RW (2012) Inertia, damping, and wave excitation of heaving coaxial cylinders. In: Proceedings of the ASME 31st international conference on ocean, offshore and arctic engineering. Rio de Janeiro, Brazil, pp 803–813. https://doi.org/10.1115/OMAE2012-83987

Falcão AFO, Henriques JCC, Cândido JJ (2012) Dynamics and optimization of the OWC spar buoy wave energy converter. Renew Energy 48:369–381. https://doi.org/10.1016/j.renene.2012.05.009

Faltinsen OM, Rognebakke OF, Timokha AN (2007) Two-dimensional resonant piston-like sloshing in a moonpool. J Fluid Mech 575:359–397. https://doi.org/10.1017/S002211200600440X

Faltinsen OM, Timokha AN (2015) On damping of two-dimensional piston-mode sloshing in a rectangular moonpool under forced heave motions. J Fluid Mech 772:R1. https://doi.org/10.1017/jfm.2015.234

Fredriksen AG, Kristiansen T, Faltinsen OM (2014) Wave-induced response of a floating two-dimensional body with a moonpool. Phil Trans R Soc A 373:20140109. https://doi.org/10.1098/rsta.2014.0109

Hamilton JA, Yeung RW (2003) Spectral shell and perfectly transparent open-boundary condition for unsteady wave-body interactions. J Offshore Mech Arct Eng 125(1):9–16. https://doi.org/10.1115/1.1537721

Haskind MD (1957) The exciting forces and wetting of ships in waves. Izv Akad Nauk SSSR, Otd Tekh Nauk 7:65–79

Kristiansen T, Faltinsen OM (2012) Gap resonance analyzed by a new domain-decompositionmethod combining potential and viscous flow. Appl Ocean Res 34:198–208. https://doi.org/10.1016/j.apor.2011.07.001

Kristiansen T, Sauder T, Firoozkoohi R (2013) Validation of a hybrid code combining potential and viscous flow with application to 3D moonpool. In: Proceedings of the ASME 2013 32nd international conference on ocean, offshore and arctic engineering. Nantes, France, V009T12A029. https://doi.org/10.1115/OMAE2013-10748

Lee M-Y (1985) Unsteady fluid-structure interaction in water of finite depth. PhD thesis, University of California, Berkeley

Matsui T, Kato K (1991) The analysis of waveinduced dynamics of ocean platforms by hybrid integral equation method. Int J Offshore Polar Eng 1(2):146–153

Matsui T, Kato K, Shirai T (1987) A hybrid integral equation method for diffraction and radiation of water waves by three-dimensional bodies. Comput Mech 2(2):119–135

Mavrakos SA (1988) Hydrodynamic coefficients for a thick-walled bottomless cylindrical body floating in water of finite depth. Ocean Eng 15(3):213–229. https://doi.org/10.1016/0029-8018(88)90040-6

Mavrakos SA (2004) Hydrodynamic coefficients in heave of two concentric surface-piercing truncated circular cylinders. Appl Ocean Res 26:84–97. https://doi.org/10.1016/j.apor.2005.03.002

McIver P (2005) Complex resonances in the water-wave problem for a floating structure. J Fluid Mech 536:423–443. https://doi.org/10.1017/S0022112005005021

McIver P, McIver M (2007) Motion trapping structures in the three-dimensional water-wave problem. J Eng Math 58(1-4):67–75. https://doi.org/10.1007/s10665-006-9103-9

Molin B (2001) On the piston and sloshing modes in moonpools. J Fluid Mech 430:27–50. https://doi.org/10.1017/S0022112000002871

Molin B, Zhang X, Huang H, Remy F (2018) On natural modes in moonpools and gaps in finite depth. J Fluid Mech 840:530–554. https://doi.org/10.1017/jfm.2018.69

Newman JN (1999) Radiation and diffraction analysis of the McIver toroid. J Eng Math 35(1):135–147. https://doi.org/10.1023/A:1004391615875

Shipway BJ, Evans DV (2003) Wave trapping by axisymmetric concentric cylinders. J Offshore Mech Arctic Eng 125:59–64. https://doi.org/10.1115/1.1537727

Wang L, Son D, Yeung RW (2016) Effect of mooring-line stiffness on the performance of a dual coaxial-cylinder wave-energy converter. Appl Ocean Res 59:577–588. https://doi.org/10.1016/j.apor.2016.07.014

Wehausen JV (1971) The motion of floating bodies. Ann Rev Fluid Mech 3(1):237–268. https://doi.org/10.1146/annurev.fl.03.010171.001321

Wehausen JV, Webster WC, Yeung RW (2016) Hydrodynamics of ships and ocean systems, lecture notes for course ME241. University of California, Berkeley. Revised

Yeung RW (1975) A hybrid integral-equation method for time-harmonic free-surface flow. In: Proceedings of the first international conference on numerical ship hydrodynamics. Gaithersburg, Maryland, USA, pp 581–607

Yeung RW (1981) Added mass and damping of a vertical cylinder in finite-depth waters. Appl Ocean Res 3(3):119–133. https://doi.org/10.1016/0141-1187(81)90101-2

Yeung RW (1985) A comparative evaluation of numerical methods in free-surface flows. In: Hydrodynamics of ocean-wave utilization, IUTAM symposium, Lisbon, Portugal. Springer-Verlag, Berlin, pp 325–356

Yeung RW, Bouger YC (1979) A hybrid integralequation method for steady two-dimensional ship waves. Int J Numer Meth Eng 14(3):317–336. https://doi.org/10.1002/nme.1620140303

Yeung RW, Seah RKM (2007) On Helmholtz and higher-order resonance of twin floating bodies. J Eng Math 58(1-4):251–265. https://doi.org/10.1007/s10665-006-9109-3

Yuen MMF, Chau FP (1987) A hybrid integral equation method for wave forces on three-dimensional offshore structures. J Offshore Mech Arct Eng 109(3):229–236. https://doi.org/10.1115/1.3257014

Zhang X, Bandyk P (2013) On two-dimensional moonpool resonance for twin bodies in a two-layer fluid. Appl Ocean Res 40:1–13. https://doi.org/10.1016/j.apor.2012.11.004

Zhang X, Bandyk P (2014) Two-dimensional moonpool resonance for interface and surface-piercing twin bodies in a two-layer fluid. Appl Ocean Res 47:204–218. https://doi.org/10.1016/j.apor.2014.05.005